#### **PAPER**

# Correlating electronic properties with M-site composition in solid solution ${\rm Ti}_y{\rm Nb}_{2-y}{\rm CT}_x$ MXenes

To cite this article: Yizhou Yang et al 2023 2D Mater. 10 014011

View the article online for updates and enhancements.

#### You may also like

- Layered ternary M<sub>n+t</sub>AX<sub>n</sub> phases and their 2D derivative MXene: an overview from a thin-film perspective
- Per Eklund, Johanna Rosen and Per O Å
  Persson
- Physical properties of 2D MXenes: from a theoretical perspective
   Aurélie Champagne and Jean-Christophe Charlier
- Exploring MXene-based materials for nextgeneration rechargeable batteries Yuanji Wu, Yingjuan Sun, Jiefeng Zheng et al

#### 2D Materials



14 August 2022

REVISED 24 October 2022

ACCEPTED FOR PUBLICATION 28 October 2022

PUBLISHED

11 November 2022

#### **PAPER**

### Correlating electronic properties with M-site composition in solid solution Ti<sub>y</sub>Nb<sub>2-y</sub>CT<sub>x</sub> MXenes

Yizhou Yang¹, Meikang Han¹,², , Christopher E Shuck¹, , Raj K Sah³, Jay R Paudel³, Alexander X Gray³, Yury Gogotsi<sup>1,2</sup> and Steven J May<sup>1,\*</sup>

- Department of Materials Science and Engineering, Drexel University, Philadelphia, PA 19014, United States of America
- A.J. Drexel Nanomaterials Institute, Drexel University, Philadelphia, PA 19104, United States of America
- Department of Physics, Temple University, Philadelphia, PA 19122, United States of America
- Author to whom any correspondence should be addressed.

E-mail: sjm95@drexel.edu

Keywords: MXene, electronic transport, conductivity, solid solution

Supplementary material for this article is available online

#### Abstract

High electrical conductivity is desired in MXene films for applications such as electromagnetic interference shielding, antennas, and electrodes for electrochemical energy storage and conversion applications. Due to the acid etching-based synthesis method, it is challenging to deconvolute the relative importance that factors such as chemical composition and flake size contribute to resistivity. To understand the intrinsic and extrinsic contributions to the macroscopic electronic transport properties, a systematic study controlling compositional and structural parameters was conducted with eight solid solutions in the  $Ti_{\nu}Nb_{2-\nu}CT_{x}$  system. In particular, we investigated the different roles played by metal (M)-site composition, flake size, and d-spacing on macroscopic transport. Hard x-ray photoemission spectroscopy and spectroscopic ellipsometry revealed changes to electronic structure induced by the M-site alloying. Consistent with the spectroscopic results, the low- and room-temperature conductivities and effective carrier mobility are correlated with the Ti content, while the impact of flake size and d-spacing is most prominent in low-temperature transport. The results provide guidance for designing and engineering MXenes with a wide range of conductivities.

#### 1. Introduction

The two-dimensional material family of MXenes has attracted significant interest in the past decade owing to their scalable synthesis and excellent performance in a variety of applications, including supercapacitors [1-5], catalysts [6-11], antennas [12, 13], and electromagnetic interference shielding [14-17]. MXenes have the general chemical composition of  $M_{n+1}X_nT_x$  where M is an early transition metal (such as Ti, Nb, and V), X is C and/or N, and  $T_x$  are the surface terminations (such as =0, -F, and -OH) that are attached to the external M layers, and n = 1-4 [18, 19]. Recently, attention has focused on the use of multiple M elements to control MXenes properties. Depending on the specific chemistry and structure, MXenes with two metals occupying the M-sites can have ordered or disordered structures [20–22]. The disordered, or solid-solution,

MXenes have both metals randomly occupying the M-site lattice, allowing for continuous variation of the composition and, thus, potentially functional properties, such as conductivity [23]. Initial studies of solid solution MXenes have shown a compositional dependence of electrochemical, electrical, optical, and catalytic properties [23-26]. In particular, the ability to directly tune electrical conductivity through M-site alloying would be impactful because many MXene applications rely on high conductivity. However, from these initial studies, it is not yet clear how each aspect of MXene chemistry (M-site, surface termination, and intercalants) affects the macroscopic electronic transport. Beyond the chemical composition and MXene structure, other factors such as defect density, flake size, and interlayer spacing (d-spacing), which may depend on MXene composition, have also been shown to modify electrical conductivity [21]. The impact of these factors

2D Mater. 10 (2023) 014011 Y Yang et al

relative to compositional alloying remains largely unexplored.

Previous studies have demonstrated that resistivity depends on the MXene chemistry. For instance, Anasori et al compared Ti<sub>3</sub>C<sub>2</sub>T<sub>x</sub>, Mo<sub>2</sub>TiC<sub>2</sub>T<sub>x</sub>, and  $Mo_2Ti_2C_3T_x$  and found that the Mo-contained MXenes have higher resistivities than  $Ti_3C_2T_x$  at both room temperature and low temperature [27].  $Mo_{1.33}CT_x$  was shown to have a room temperature resistivity of 3.4  $\times$  10<sup>-3</sup>  $\Omega$  cm, which is 4 orders of lower than  $Mo_2CT_x$  [28–30]. In addition to the M-site, X-site variation also leads to a change in resistivity [31]. For Ti<sub>3</sub>CNT<sub>x</sub>, the lowest roomtemperature resistivity reported is  $2.00 \times 10^{-2} \Omega$  cm, which was achieved by HF etching followed by tetramethylammonium hydroxide (TMAOH) delamination [32]. In contrast, the resistivities for  $Ti_3C_2T_x$  films range from 8.0  $\times$  10<sup>-3</sup>  $\Omega$  cm to  $5.0 \times 10^{-5} \Omega$  cm [33–41]. Moreover, spectroscopic evidence reveals that M-site chemistry affects the electronic structure. Ultraviolet-visible-near infrared (UV-vis-NIR) spectroscopy shows different plasmon resonance peaks in  $Ti_3C_2T_x$ ,  $Mo_2CT_x$ ,  $Mo_2TiC_2T_x$ ,  $Ti_2CT_x$ , and  $Nb_2CT_x$  from 450 nm to 951 nm [42]. Normalized optical spectra exhibit systematic changes in extinction coefficient of M<sub>2</sub>CT<sub>x</sub> where the M-site elements are Ti, Nb, and/or V [23]. Electron energy loss spectroscopy [43] and x-ray absorption spectroscopy [23] also were used to demonstrate that the secondary M-site variation in solid solutions contribute to changes in intrinsic band structure. Density functional theory studies also show systematic changes to electronic structure by M-site alteration and number of layers in MXenes [44–48].

It was also demonstrated that additional factors related to morphology or disorder (which we refer to as extrinsic factors) including average flake size and dspacing affect the resistivity. Because resistivity measurements performed on MXene films probe ensemble behavior as current passes through many discontinuous flakes, both inter- and/or intra-flake scattering mechanisms contribute to electrical conductivity. One would then expect that these mechanisms are, at least partially, dependent on the average flake size. Multiple reports have shown that larger flake sizes lead to better conductivity [49–51]. For instance, Maleski et al reported the room temperature conductivity of Ti<sub>3</sub>C<sub>2</sub>T<sub>r</sub> films decreased by a factor of two when the flake size was decreased from 4.4 µm to 0.13 µm [52]. However, the limiting electron interflake hopping mechanism is still unresolved because electron hops can be vertical, occurring over the interlayer spacing ( $=d_{002}$ ), or lateral, as electrons tunnel between edges of adjacent flakes, occurring with a frequency that should scale inversely to the flake size. However, in some well-optimized MXenes, it appears that transport is not limited by inter-flake scattering. In  $Ti_3C_2T_x$ , the room temperature conductivity of high-quality freestanding films (comprised of many stacked flakes) [33] is equivalent to single flake samples [53, 54], indicating that transport in these MXenes is dominated by intraflake scattering and their intrinsic electronic structure. Besides the flake size, the d-spacing also affects the electronic properties. Resistivity can depend on interlayer spacing, which is primarily determined by intercalants such as water, Li<sup>+</sup>, tetramethylammonium (TMA<sup>+</sup>), tetrabutylammonium (TBA<sup>+</sup>), and dimethyl sulfoxide. The removal of these intercalants by hightemperature vacuum annealing provides a means to understand the relationship between d-spacing and conductivity [55–57]. For example, Zhao et al found that the room temperature conductivity of  $Ti_3C_2T_x$ increased 2.4 times following the decrease of the interlayer spacing from 13.4 Å to 10.3 Å [35].

Herein, we present systematic electronic transport and spectroscopic measurements on a set of eight MXenes ( $Ti_v Nb_{2-v} CT_x$ ) to compare the relative impact of M-site composition (y), d-spacing, and flake size on macroscopic electronic behavior. We find that the M-site composition plays a more significant role in the room temperature transport compared to flake size and d-spacing, the impact of which is more pronounced at low temperatures. Spectroscopic measurements reveal clear shifts in spectral weights, consistent with alloying-induced changes to electronic structure and macroscopic transport. Our approach enables us to identify the relative importance of both intrinsic and extrinsic factors on different aspects of transport, both shedding light on origins of macroscopic transport features and illustrating how M-site composition can be used to engineer conductivity in MXenes.

#### 2. Results and discussion

#### 2.1. Sample structure and composition

All  $Ti_yNb_{2-y}CT_x$  films were synthesized following previous reports [23]; see SI for details. Prior to investigating the transport behavior, the sample quality was examined via x-ray diffraction and x-ray photoelectron spectroscopy (XPS). Figure 1(a) shows representative 002 peaks for each composition. All 002 peaks are located near  $2\theta = 7^{\circ}$  which agrees with other reports of  $M_2CT_x$  MXenes [23, 58]. No peaks associated with MAX phases are observed following the conversion from MAX to MXene. The 002 peaks for the other set of samples presented in this study are shown in figure S1.

Figures 1(b) and (c) show the Ti 2p and Nb 3d photoemission spectra. The Ti spectra are deconvoluted into Ti–C, Ti(II), Ti(III), and Ti–O peaks [59]. None of the samples exhibit a significant oxidation peak at 459 eV. The Nb spectra are deconvoluted into Nb- $T_x$  and Nb–C peaks. The Nb spectra show no indication of the Nb-O peak at 206.8 eV. The deconvoluted Ti 2p and Nb 3d spectra for 8 different  $Ti_vNb_{2-v}CT_x$  samples are shown in figures S2 and S3.

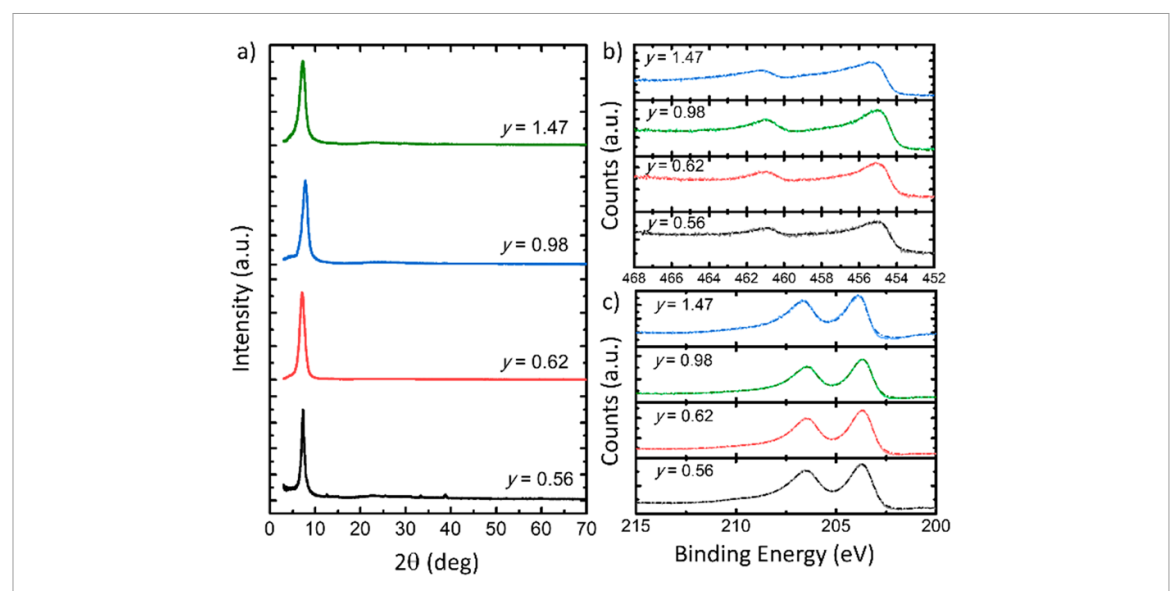


**Figure 1.** (a) X-ray diffraction patterns showing the 002 peak for  $\text{Ti}_y \text{Nb}_{2-y} \text{CT}_x$  samples. Core level XPS spectra for (b) Ti 2p and (c) Nb 3d, the solid lines represent the measured spectra and dashed lines represent the fitted spectra.

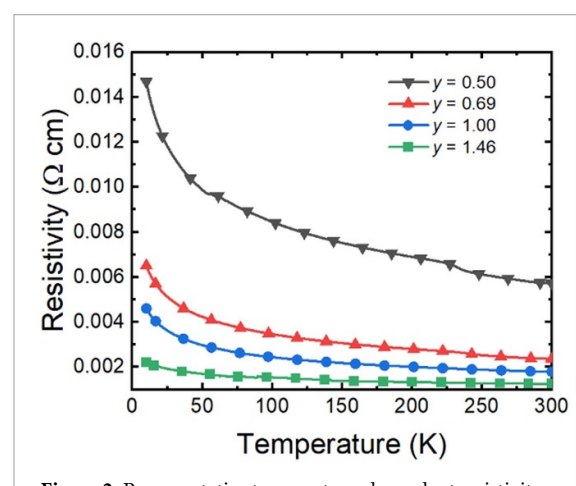


**Figure 2.** Representative temperature-dependent resistivity data for different compositions made within the same synthesis batch.

The bonding assignments attributed within the XPS data are based on previous studies of  $(Ti,Nb)_2CT_x$ ,  $Nb_2CT_x$ , and  $Nb_4C_3T_x$  [23, 60, 61]. The Ti and Nb bonds with carbon and surface termination are similar across the four different compositions, indicating that no sample is significantly more oxidized than the other samples. The stoichiometry of the samples is determined from the photoemission spectra. The surface termination (Cl, F, and O) concentrations are quantified based on XPS; no trend of the surface termination concentration is observed as a function of y, as shown in table S1. As all the samples are synthesized through the LiF + HCl etching method, the d-spacing is not expected to change from batch to batch, but is not purposely controlled.

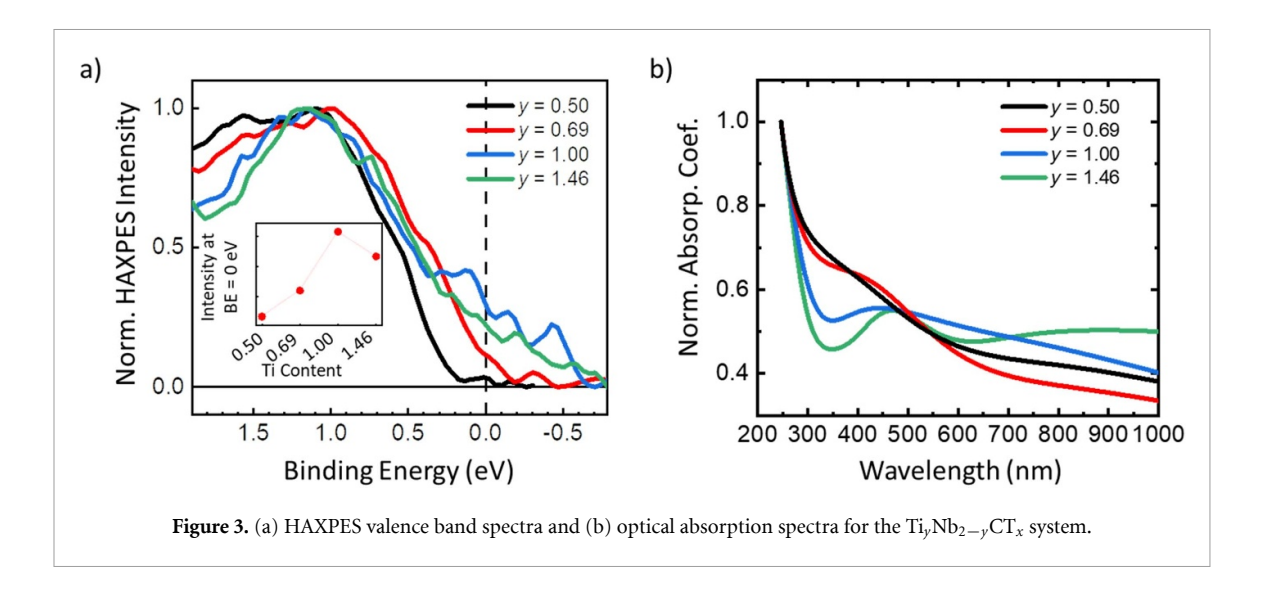
#### 2.2. Macroscopic electronic transport

The temperature-dependent resistivity of  $\text{Ti}_{y}\text{Nb}_{2-y}\text{C}_{2}\text{T}_{x}$  films is presented in figure 2. Similar

to the initial report of this material family [23], as the Ti concentration is increased (as y is increased), the resistivity decreases at both 300 and 10 K; the magnitude of the conductivity for these samples is increased compared to our initial report [23] owing to improvements in material quality. Other batches of Ti<sub>y</sub>Nb<sub>2-y</sub>C<sub>2</sub>T<sub>x</sub> samples, all synthesized under identical conditions, show the same resistivity trends (figure S4(a)), though the exact resistivity magnitudes vary from batch to batch. This trend can also be extended to the end compounds  $Ti_2CT_x$  and  $Nb_2CT_x$ , which were reported to have resistivity values of  $4.4 \times 10^{-4} \Omega$  cm and  $0.04 \Omega$  cm at room temperature, respectively [58]. Because  $Ti_2CT_x$  is readily oxidized in air and Nb<sub>2</sub>CT<sub>x</sub> requires different synthesis approaches than Ti<sub>v</sub>Nb<sub>2-y</sub>CT<sub>x</sub> samples, we focus our attention on the double-M alloys, which can all be synthesized using the same method, yielding material of similar quality. It is also noteworthy that the lowtemperature resistivities differ more substantially as a function of y than the room temperature resistivity; figure S4(b) shows the resistivity normalized to the room-temperature. Having established that the resistivity does systematically depend on the Ti:Nb ratio, we next identify if these conductivity changes are driven by intrinsic changes to the electronic structure or arise from changes to extrinsic material factors that are altered unintentionally through changes to the M-site composition.

#### 2.3. Spectroscopic probes of intrinsic contributions

Electronic structure and density of states (DOS) near the Fermi level are the most important intrinsic factors that directly contribute to electronic transport properties. To probe the DOS experimentally, valence-band spectra of all four samples were measured using bulk-sensitive hard x-ray photoemission



spectroscopy (HAXPES) with an excitation energy of 5.41 keV and a resolution of 0.4 eV. Figure 3(a) shows the near-Fermi-edge region of the spectra, normalized to the peak intensity at approximately 1 eV binding energy. The spectrum for the sample with the lowest Ti content  $(Ti_{0.5}Nb_{1.5}CT_x)$  exhibits the sharpest cut-off of the valence-band maximum with a near-zero DOS at the Fermi level. For the rest of the samples, a significant increase in the DOS spectral weight is observed near the Fermi level with increasing Ti content. The trend, which is shown in the inset of figure 3(a), is systematic with the exception of  $Ti_{1.0}Nb_{1.0}CT_x$ , which is more resistive than  $Ti_{1.46}Nb_{0.54}CT_x$  but exhibits a slightly higher DOS spectral weight near the Fermi level.

The second main conclusion that can be drawn from the HAXPES is that for the solid solutions, the Fermi level lays within an energy band and thus the material is not a semiconductor. From the resistivity data in figure 2, it is noticeable that all four compositions have a negative  $d\rho/dT$  value. This behavior is commonly seen in many other MXenes and is attributed to extrinsic factors such as disorder and inter-flake hopping [29, 57, 58, 62–64]. However, the valence band spectra make clear that the negative  $d\rho/dT$  does not originate from thermal excitation of carriers across a band gap. This is also consistent with the modest, non-exponential increase in resistivity with decreasing temperature.

Spectroscopic ellipsometry is another technique that probes the intrinsic electronic structure of materials. The absorption spectra are shown in figure 3(b), which are calculated from the extinction coefficient (*k*), providing information regarding intrinsic electronic features such as plasmonic resonances and inter-band transitions. Each composition has an absorption peak between 350 nm and 550 nm. With increasing Ti content, the peak position moves towards higher wavelength. While assigning a specific physical origin to the spectral features is beyond the scope of this work, it is clear that a systematic change

in the optical spectra results from the substitution of the transition metal. Therefore, the optical spectra provide direct evidence that M-site alloying is altering the intrinsic electronic structure. The trend in the absorption results is consistent with the previous extinction coefficients measured by UV–vis from MXene solutions [23]. While the spectroscopic results indicate compositionally-induced changes in the electronic structure, these results do not establish causation of the resistivity trends as other independent parameters could also be modified with M-site substitution.

## 2.4. Extrinsic and intrinsic contributions to transport

To understand the relative impact of the flake size on the conductivity, a set of  $Ti_{1.0}Nb_{1.0}CT_x$  films with systematically varied flake sizes was prepared and characterized. The flake size was controlled by sonication time during synthesis. The flake size was measured via dynamic light scattering, see SI for details. More details on the dependence of the flake size on sonication time can be found in table S2. The temperature-dependent resistivity for the isocompositional sample set is provided in figure S5.

We collected compositional, structural, and transport data from 17 samples, which are divided into two sets. The first set of samples includes eight individual  $\mathrm{Ti}_y\mathrm{Nb}_{2-y}\mathrm{CT}_x$  films with varying y (y-set), while the second set of samples includes nine iso-compositional films with different flake sizes. All 17 samples were used for d-spacing analysis. By performing linear regression analysis on the two data sets, the quantitative relationship between the macroscopic transport properties and the compositional and structural contributions can be described by correlation (R) and the p-value (p). The summary of sample data and the fitted statistical constants is shown in figure 4.

To understand the macroscopic transport properties of  $\text{Ti}_y \text{Nb}_{2-y} \text{CT}_x$ , the effective carrier mobility  $(\mu)$ , the room temperature resistivity  $(\rho_{300\text{K}})$ ,

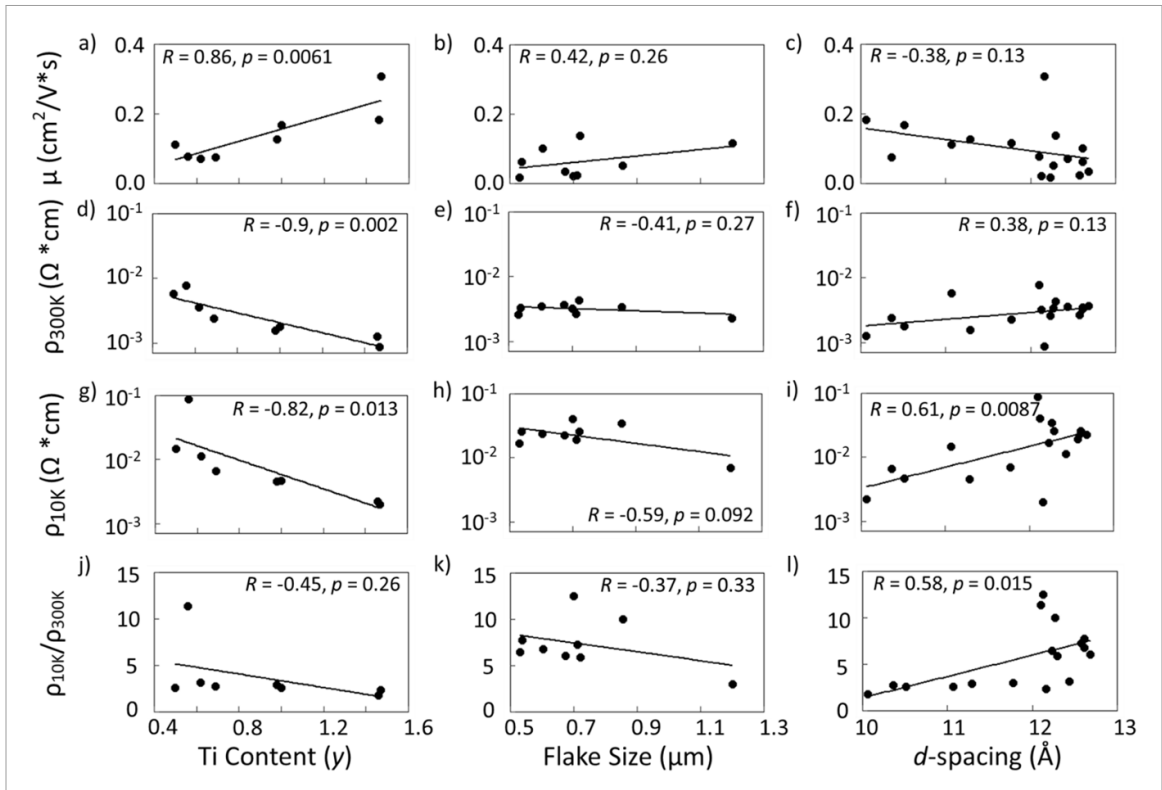


**Figure 4.** Correlation plots for Ti content, flake size, and d-spacing dependence of the carrier mobilities, room temperature and 10 K resistivities, and the ratio of the 10 K and 300 K resistivity. A linear regression is used to analyze the statistical relationship. R is the correlation and p is the confidence level.

the low temperature resistivity ( $\rho_{10K}$ ), and the ratio of low-to-room temperature resistivity ( $\rho_{10K}/\rho_{300K}$ ) were measured. The carrier mobility, here measured at 10 K, provides a measure of carrier scattering via defects, surfaces, and flake-to-flake hopping processes. Mobility is obtained directly from the Hall coefficient and the longitudinal resistance, and thus has the advantage of being thickness independent. Given that these MXenes are intrinsically metallic, they should exhibit  $\rho_{10K}/\rho_{300K}$  values that are less than 1. Values larger than 1, therefore, indicate an increased role of extrinsic transport mechanisms such as inter-flake scattering or disorder-induced hopping that result in negative  $d\rho/dT$  behavior [29, 57, 58, 62–64].

To directly compare various aspects of the electronic behavior, the change ( $\Delta$ ) in  $\mu$ ,  $\rho_{300K}$ ,  $\rho_{10K}$ , and  $\Delta\rho_{10K}/\rho_{300K}$  were calculated.  $\Delta$  values are defined by subtracting the minimal value from the maximum value. All the  $\Delta$  values except  $\rho_{10K}/\rho_{300K}$  are larger with change of y content (y ranges from 0.5 to 1.47) than the changes that were induced by flake size (flake size ranges from 0.5  $\mu$ m to 1.2  $\mu$ m), indicating that the change in composition has a greater impact on transport than the change in flake size. The measured  $\Delta$  values are listed in table 1.

The Pearson correlation coefficient (R) was calculated for the various data sets to understand the degree of correlation between the transport properties and y, flake size, and d-spacing. In this case,

**Table 1.** The change in  $\mu$  (cm<sup>2</sup> V<sup>-1</sup> s<sup>-1</sup>),  $\rho_{300K}$  ( $\Omega$  cm),  $\rho_{10K}$  ( $\Omega$  cm), and  $\Delta\rho_{10K}/\rho_{300K}$  for y set samples, iso-compositional set samples, and all samples.

	<i>y</i> ( <i>y</i> set)	flake size (iso- compositional set)	d-spacing (including all samples)
$\Delta \mu$	0.23	0.12	0.29
$\Delta \rho_{300\mathrm{K}}$	0.0069	0.0020	0.0069
$\Delta  ho_{10\mathrm{K}}$	0.086	0.034	0.086
$\Delta \rho_{10\mathrm{K}}/\rho_{300\mathrm{K}}$	9.6	9.4	10.7

we use R to identify the correlations between the independent variables (y, flake size, and the dspacing) and the electronic parameters. Conventionally, for R values above 0.65, the correlations can be defined as 'moderate' and 'strong' according to the Pearson correlation interpretation [65]. By comparing R, the level of contribution can be quantified for each electronic property. The R values for the y dependence are 0.86 for  $\mu$ , 0.9 for  $\log(\rho_{300K})$ , and 0.82 for  $\log(\rho_{10\text{K}})$ . These high values indicate the M-site composition is linearly correlated with these electronic characteristics at both room temperature and low temperature. However, the *R* for the *y* dependence of  $\rho_{10\text{K}}/\rho_{300\text{K}}$  is only 0.45, suggesting y contributes less to the shape of  $d\rho/dT$ . In contrast, the R values for flake size dependence is 0.42 for  $\mu$ , 0.41 for log( $\rho_{300\text{K}}$ ) and 0.59 for log( $\rho_{10\text{K}}$ ). Therefore, for this system, the flake size is not as linearly

**Table 2.** The absolute R value for each independent and dependent variable. Darker green filling corresponds to higher correlations. p values are indicated with bold and underlines. (p < 0.05, bold; 0.05 , underline; <math>p > 0.1, no underline).

	Ti Content (y)	Flake Size (µm)	d-spacing (Å)
$\mu (\text{cm}^2  \text{V}^{-1} \times \text{s}^{-1})$	0.86	0.42	0.38
$\rho_{300K}$ (Ohm × cm)	0.9	0.41	0.38
$\rho_{10K}$ (Ohm × cm)	0.82	0.59	0.61
$ ho_{10\mathrm{K}}/ ho_{300\mathrm{K}}$	0.45	0.37	0.58

correlated with the electronic transport properties as the M-site composition. It is noteworthy that the R value obtained from the flake size data set is largest for the low temperature resistivity, suggesting that the flake size contribution becomes more significant at low temperature. In the d-spacing analysis, the R value is the largest for the  $\rho_{10\rm K}/\rho_{300\rm K}$  ratio, suggesting that the interlayer distance plays an increasingly important role on the shape of  $\mathrm{d}\rho/\mathrm{d}T$ .

To examine the R value confidence, p values, which test the statistical significance, were calculated. Values of p < 0.05 suggest the null hypothesis is rejected, while p > 0.1 suggests no evidence against the null hypothesis. In other words, lower p values indicate greater statistical significance. The obtained p values are shown in figure 4, as well as indicated in table 2. This analysis helps to deconvolute the different contributions to the overall macroscopic resistivity of this MXene system. It is noteworthy that in this study, we have only examined linear correlations. For *p* values that are higher than 0.1, there could be non-linear correlations between the material parameter and the electronic properties. More sophisticated models with larger data sets could shed light on this in the future studies.

We find that the overall electronic behavior in these  $Ti_{\nu}Nb_{2-\nu}CT_{x}$  solid solution samples is dominated by the composition itself, especially at room temperature. However, the trends observed as a function of flake size and d-spacing make clear that it is also important to optimize the sample quality in order to achieve better metallic properties. For instance, the low temperature carrier mobility tends to increase with increasing flake size, independent of M-site composition. The results also show that the M-site composition tends to shift the whole temperaturedependent resistivity curve vertically, while the flake size and d-spacing tend to alter the shape of the resistivity curve by increasing the low temperature slope more directly than the room temperature slope. This approach can be extended to other MXene systems with two or more elements in the M-site to

isolate the impact of composition from microstructural features. To design new MXenes for applications with specific resistivity, having a second metal to form solid solution MXenes can be a promising path.

#### 3. Conclusion

Our systematic study of the electronic transport properties of eight Ti<sub>y</sub>Nb<sub>2-y</sub>CT<sub>x</sub> solid solution MXenes via HAXPES and statistical analysis of macroscopic transport data based on three material variables shows that macroscopic electronic transport is highly correlated with the Ti content. The relative significance of the flake size and d-spacing increases at low temperature, leading to changes in  $d\rho/dT$  driven largely by increased low temperature resistivity. The HAXPES and optical measurements clearly reveal that Ti:Nb alloying induces systematic changes to the electronic structure of  $Ti_{\nu}Nb_{2-\nu}CT_{x}$ , consistent with the increased conductivity as y is increased. This work provides guidance for future MXene exploration, yielding insight into how M-site compositional tuning alters different aspects of electronic behavior.

#### Data availability statement

The data that support the findings of this study are available upon reasonable request from the authors.

#### Acknowledgments

Electronic transport, data analysis, and optical spectroscopy measurements performed at Drexel University were supported by the U.S. Department of Energy (DOE), Office of Science, Office of Basic Energy Sciences, grant #DE-SC0018618. Research on synthesis of MXene solid solutions at Drexel was supported by the U S. National Science Foundation (Ceramics Program) Grant DMR-2041050. M H, C S, and Y G acknowledge support from the U.S. National Science Foundation (grants ECCS-2034114 and DMR-2041050). A X G, J R P and R K S acknowledge support from the DOE, Office of Science, Office of Basic Energy Sciences, Materials Sciences, and Engineering Division under Award No. DE-SC0019297. The electrostatic photoelectron analyzer for the lab based HAXPES measurements at Temple University was acquired through an Army Research Office DURIP grant (Grant No. W911NF-18-1-0251). Kanit Hantanasirisakul and Mark Anayee (Drexel University) are acknowledged for helping with XPS measurement and analysis. Drexel University Materials Characterization Core Facilities is acknowledged for providing access to XRD and XPS instruments.

2D Mater. 10 (2023) 014011 Y Yang et al

#### **ORCID** iDs

Christopher E Shuck https://orcid.org/0000-0002-1274-8484

Yury Gogotsi https://orcid.org/0000-0001-9423-4032

Steven J May https://orcid.org/0000-0002-8097-1549

#### References

- [1] Ghidiu M, Lukatskaya M R, Zhao M-Q, Gogotsi Y and Barsoum M W 2014 Nature 516 78
- [2] Lin S-Y and Zhang X 2015 J. Power Sources 294 354-9
- [3] Guo M, Liu C, Zhang Z, Zhou J, Tang Y and Luo S 2018 Adv. Funct. Mater. 28 1803196
- [4] Yang C, Tang Y, Tian Y, Luo Y, Faraz Ud Din M, Yin X and Que W 2018 Adv. Energy Mater. 8 1802087
- [5] Boota M and Gogotsi Y 2019 Adv. Energy Mater. 9 1802917
- [6] Seh Z W, Fredrickson K D, Anasori B, Kibsgaard J, Strickler A L, Lukatskaya M R, Gogotsi Y, Jaramillo T F and Vojvodic A 2016 ACS Energy Lett. 1 589–94
- [7] Liu J, Liu Y, Xu D, Zhu Y, Peng W, Li Y, Zhang F and Fan X 2019 Appl. Catal. B 241 89–94
- [8] Pang S-Y, Wong Y-T, Yuan S, Liu Y, Tsang M-K, Yang Z, Huang H, Wong W-T and Hao J 2019 J. Am. Chem. Soc. 141 9610–6
- [9] Xiu L, Pei W, Zhou S, Wang Z, Yang P, Zhao J and Qiu J 2020 Adv. Funct. Mater. 30 1910028
- [10] Yan L, Zhang B, Wu S and Yu J 2020 J. Mater. Chem. A 8 14234–42
- [11] Li K, Lu X, Zhang Y, Liu K, Huang Y and Liu H 2020 Environ. Res. 185 109409
- [12] Sarycheva A, Polemi A, Liu Y, Dandekar K, Anasori B and Gogotsi Y 2018 Sci. Adv. 4 eaau0920
- [13] Han M, Liu Y, Rakhmanov R, Israel C, Tajin M A S, Friedman G, Volman V, Hoorfar A, Dandekar K R and Gogotsi Y 2021 Adv. Mater. 33 2003225
- [14] Shahzad F, Alhabeb M, Hatter C B, Anasori B, Hong S M, Koo C M and Gogotsi Y 2016 *Science* 353 1137–40
- [15] Uzun S, Han M, Strobel C J, Hantanasirisakul K, Goad A, Dion G and Gogotsi Y 2021 Carbon 174 382–9
- [16] Iqbal A, Shahzad F, Hantanasirisakul K, Kim M-K, Kwon J, Hong J, Kim H, Kim D, Gogotsi Y and Koo Chong M 2020 Science 369 446–50
- [17] Han M, Shuck C E, Rakhmanov R, Parchment D, Anasori B, Koo C M, Friedman G and Gogotsi Y 2020 ACS Nano 14 5008–16
- [18] Naguib M, Kurtoglu M, Presser V, Lu J, Niu J, Heon M, Hultman L, Gogotsi Y and Barsoum M W 2011 Adv. Mater. 23 4248–53
- [19] Deysher G et al 2020 ACS Nano 14 204-17
- [20] Anasori B, Xie Y, Beidaghi M, Lu J, Hosler B C, Hultman L, Kent P R, Gogotsi Y and Barsoum M W 2015 ACS Nano 9 9507–16
- [21] Shekhirev M, Shuck C E, Sarycheva A and Gogotsi Y 2021 Prog. Mater. Sci. 120 100757
- [22] Dahlqvist M and Rosen J 2020 Nanoscale 12 785-94
- [23] Han M et al 2020 J. Am. Chem. Soc. 142 19110-8
- [24] Shen Z, Wang Z, Zhang M, Gao M, Hu J, Du F, Liu Y and Pan H 2018 *Materialia* 1 114–20
- [25] Li P, Zhu J, Handoko A D, Zhang R, Wang H, Legut D, Wen X, Fu Z, Seh Z W and Zhang Q 2018 J. Mater. Chem. A 6 4271–8
- [26] Wang L, Han M, Shuck C E, Wang X and Gogotsi Y 2021 Nano Energy 88 106308

- [27] Anasori B, Shi C, Moon E J, Xie Y, Voigt C A, Kent P R, May S J, Billinge S J, Barsoum M W and Gogotsi Y 2016 Nanoscale Horiz. 1 227–34
- [28] Tao Q et al 2017 Nat. Commun. 8 14949
- [29] Halim J et al 2016 Adv. Funct. Mater. 26 3118-27
- [30] Zhu S et al 2022 Adv. Mater. 34 2108809
- [31] Huang K, Li Z, Lin J, Han G and Huang P 2018 *Chem. Soc. Rev.* 47 5109–24
- [32] Hantanasirisakul K et al 2019 Chem. Mater. 31 2941-51
- [33] Mathis T S, Maleski K, Goad A, Sarycheva A, Anayee M, Foucher A C, Hantanasirisakul K, Shuck C E, Stach E A and Gogotsi Y 2021 ACS Nano 15 6420–9
- [34] Zhao M Q, Ren C E, Ling Z, Lukatskaya M R, Zhang C, Van Aken K L, Barsoum M W and Gogotsi Y 2015 Adv. Mater. 27 339–45
- [35] Zhao X, Wang Z, Dong J, Huang T, Zhang Q and Zhang L 2020 J. Power Sources 470 228356
- [36] Chen J, Yang B, Lim Y D, Duan W, Zhao Y, Tay B K and Yan X 2020 Nanotechnology 31 285701
- [37] Chen H, Wen Y, Qi Y, Zhao Q, Qu L and Li C 2020 Adv. Funct. Mater. 30 1906996
- [38] Yang S, Zhang P, Wang F, Ricciardulli A G, Lohe M R, Blom P W M and Feng X 2018 Angew. Chem., Int. Ed. 57 15491–5
- [39] Zhao X et al 2019 Matter 1 513-26
- [40] Mirkhani S A, Shayesteh Zeraati A, Aliabadian E, Naguib M and Sundararaj U 2019 ACS Appl. Mater. Interfaces 11 18599–608
- [41] von Treifeldt J E, Firestein K L, Fernando J F S, Zhang C, Siriwardena D P, Lewis C-E M and Golberg D V 2021 Mater. Des. 199 109403
- [42] Maleski K, Shuck C E, Fafarman A T and Gogotsi Y 2021 Adv. Opt. Mater. 9 2001563
- [43] Foucher A C, Han M, Shuck C E, Maleski K, Gogotsi Y and Stach E 2022 2D Mater. 9 025004
- [44] Khazaei M, Ranjbar A, Arai M and Yunoki S 2016 Phys. Rev. B 94 125152
- [45] Liang Y, Khazaei M, Ranjbar A, Arai M, Yunoki S, Kawazoe Y, Weng H and Fang Z 2017 Phys. Rev. B 96 195414
- [46] Weng H, Ranjbar A, Liang Y, Song Z, Khazaei M, Yunoki S, Arai M, Kawazoe Y, Fang Z and Dai X 2015 Phys. Rev. B 92 075436
- [47] Dong L, Kumar H, Anasori B, Gogotsi Y and Shenoy V B 2017 J. Phys. Chem. Lett. 8 422–8
- [48] Zhang Y, Xia W, Wu Y and Zhang P 2019 *Nanoscale* 11 3993–4000
- [49] Zhang C, Anasori B, Seral-Ascaso A, Park S-H, McEvoy N, Shmeliov A, Duesberg G S, Coleman J N, Gogotsi Y and Nicolosi V 2017 Adv. Mater. 29 1702678
- [50] Tu S, Jiang Q, Zhang J, He X, Hedhili M N, Zhang X and Alshareef H N 2019 ACS App. Mater. Interfaces 11 27358–62
- [51] Zhang J et al 2020 Adv. Mater. 32 2001093
- [52] Maleski K, Ren C E, Zhao M-Q, Anasori B and Gogotsi Y 2018 ACS Appl. Mater. Interfaces 10 24491–8
- [53] Lipatov A, Goad A, Loes M J, Vorobeva N S, Abourahma J, Gogotsi Y and Sinitskii A 2021 Matter 4 1413–27
- [54] Miranda A, Halim J, Barsoum M and Lorke A 2016 Appl. Phys. Lett. 108 033102
- [55] Qiao C, Wu H, Xu X, Guan Z and Ou-Yang W 2021 Adv. Mater. Interfaces 8 2100903
- [56] Tang H, Yang Y, Wang R and Sun J 2020 J. Mater. Chem. C 8 6214–20
- [57] Hart J L, Hantanasirisakul K, Lang A C, Anasori B, Pinto D, Pivak Y, van Omme J T, May S J, Gogotsi Y and Taheri M L 2019 Nat. Commun. 10 522
- [58] Halim J, Persson I, Moon E J, Kühne P, Darakchieva V, Persson P O Å, Eklund P, Rosen J and Barsoum M W 2019 J. Phys.: Condens. Matter 31 165301
- [59] Natu V, Benchakar M, Canaff C, Habrioux A, Celerier S and Barsoum M W 2021 Matter 4 1224–51

2D Mater. 10 (2023) 014011 Y Yang et al

[60] Kamysbayev V, Filatov A S, Hu H, Rui X, Lagunas F, Wang D, Klie R F and Talapin D V 2020 *Science* 369 979–83

- [61] Halim J, Cook K M, Naguib M, Eklund P, Gogotsi Y, Rosen J and Barsoum M W 2016 Appl. Surf. Sci. 362 406–17
- [62] Halim J, Palisaitis J, Lu J, Thörnberg J, Moon E J, Precner M, Eklund P, Persson P O Å, Barsoum M W and Rosen J 2018 ACS Appl. Nano Mater. 1 2455–60
- [63] Halim J, Moon E J, Eklund P, Rosen J, Barsoum M W and Ouisse T 2018 *Phys. Rev.* B **98** 104202
- [64] Urbankowski P, Anasori B, Hantanasirisakul K, Yang L, Zhang L, Haines B, May S J, Billinge S J and Gogotsi Y 2017 Nanoscale 9 17722–30
- [65] Hinkle D E, Wiersma W and Jurs S G 2003 Applied Statistics for the Behavioral Sciences (Boston, MA: Houghton Mifflin College Division)